Applied Catalysis B: Environmental 189 (2016) 86–98

Contents lists available at ScienceDirect

Applied Catalysis B: Environmental

journal homepage: www.elsevier.com/locate/apcatb

Catalytic and kinetic investigation of the encapsulated random alloy (Pd_n-Au_{110-n}) nanoparticles

Ali K. Ilunga, Reinout Meijboom*

Department of Chemistry, University of Johannesburg, PO Box 524, Auckland Park 2006, Johannesburg, South Africa

ARTICLE INFO

Article history:
Received 25 November 2015
Received in revised form 26 January 2016
Accepted 16 February 2016
Available online 20 February 2016

Keyword:
Dendrimer
Metal nanoparticles
Oxidation
Kinetic
Langmuir–Hinshelwood mechanism

ABSTRACT

Generation six hydroxyl terminated PAMAM dendrimer was used as template for the synthesis of several palladium-gold random alloy nanoparticles. The synthesis process was monitored using UV–spectroscopy. The microscopy image of the alloy nanoparticles was captured by transmission electron microscopy and their average size was compared to the theoretical value. Catalytic oxidation of morin by hydrogen peroxide was performed to investigate the activity of the alloy nanoparticles. The Langmuir–Hinshelwood approach was used to conduct a full kinetic evaluation of the catalytic process. The catalytic activity exhibited by the alloy nanoparticles demonstrates a proportional increase with the relative palladium amount. The encapsulated alloy and mono metal nanoparticles remained narrowly dispersed after the reaction.

1. Introduction

Interest in the use of dendrimers increases due to their architecture, physicochemical properties, and accessibility [1–3]. A dendrimer can be described as having a *pseudo*-spherical shape which consists of a steric microenvironment into which metal nanoparticles can be encapsulated. The terminal groups of the dendrimer allows the use of dendrimers in a variety of solvents and control the selected diffusion of the substrates [4]. Metal nanoparticles can be synthesized by reducing metal salts in the presence of a dendrimer. The particle size of nanoparticles can be controlled and their agglomeration prevented due to the presence of dendrimers [5]. The nanoparticles are stabilized by steric effects, which is a great advantage for their catalytic efficacy, so that the access of substrates to the catalyst surface will not be hindered [6].

Resulting from the properties which differ from their related bulk materials, the use of metal nanoparticles has expanded to diverse scientific areas such as catalysis, medicine, physics, and nanotechnology [7–11]. Among the properties or attributes which justify the catalytic application of metal nanoparticles, we list their high surface area to volume ratio, and also their lower melting point [10,12]. The size and shape of metal nanoparticles are the essential attributes which could be related to their catalytic activity.

Based on a pioneering report on dendrimer encapsulated nanoparticles (DENs) by Zhao et al. [13], a considerable number of encapsulated mono and bi-metallic nanoparticles were prepared using a dendritic template. Fundamentally, the synthesis of dendrimer encapsulated bi-metallic nanoparticles can be performed by three methods: co-complexation of metal salts, galvanic displacement and sequential reduction [14,15]. The catalytic activities of bi-metallic nanoparticles were evaluated in a variety of chemical and electrochemical reactions [16,17]. Pozun et al. reported the synthesis of random alloy bi-metallic nanoparticles using a dendritic template and their catalytic investigation following the Brønsted–Evans–Polanyi relationship [18].

Morin, a natural flavonoid isolated from plant extract, is widely used due to its pharmacological properties [19]. Among those properties were listed anti-inflammatory, hepatoprotective, antioxidant, and so on. Morin, a quercetin compound, can analytically be detected by UV–vis spectroscopy. The relative UV-absorption peak is detected at λ 410 nm [20,21]. One of the chemical characterizations of quercetin compounds is that they can be oxidized by oxidases, enzymes, and radicals [22–24]. The ortho-position of hydroxyl group R_1 in the morin structure presents great advantage in their use as model compound in catalytic investigation. The reason behind that is that this position prevents the dimerization of morin during the reaction [25].

Here, we report the synthesis of dendrimer encapsulated Pd_n-Au_{110-n} nanoparticles by co-complexation method, which results in random alloy nanoparticles. The characterization of Pd_n-Au_{110-n} were performed by UV–vis spectroscopy and high-resolution

* Corresponding author.
E-mail addresses: rmeijboom@uj.ac.za, reinout.meijboom@gmail.com (R. Meijboom).

http://dx.doi.org/10.1016/j.apcatb.2016.02.040
0926-3373/

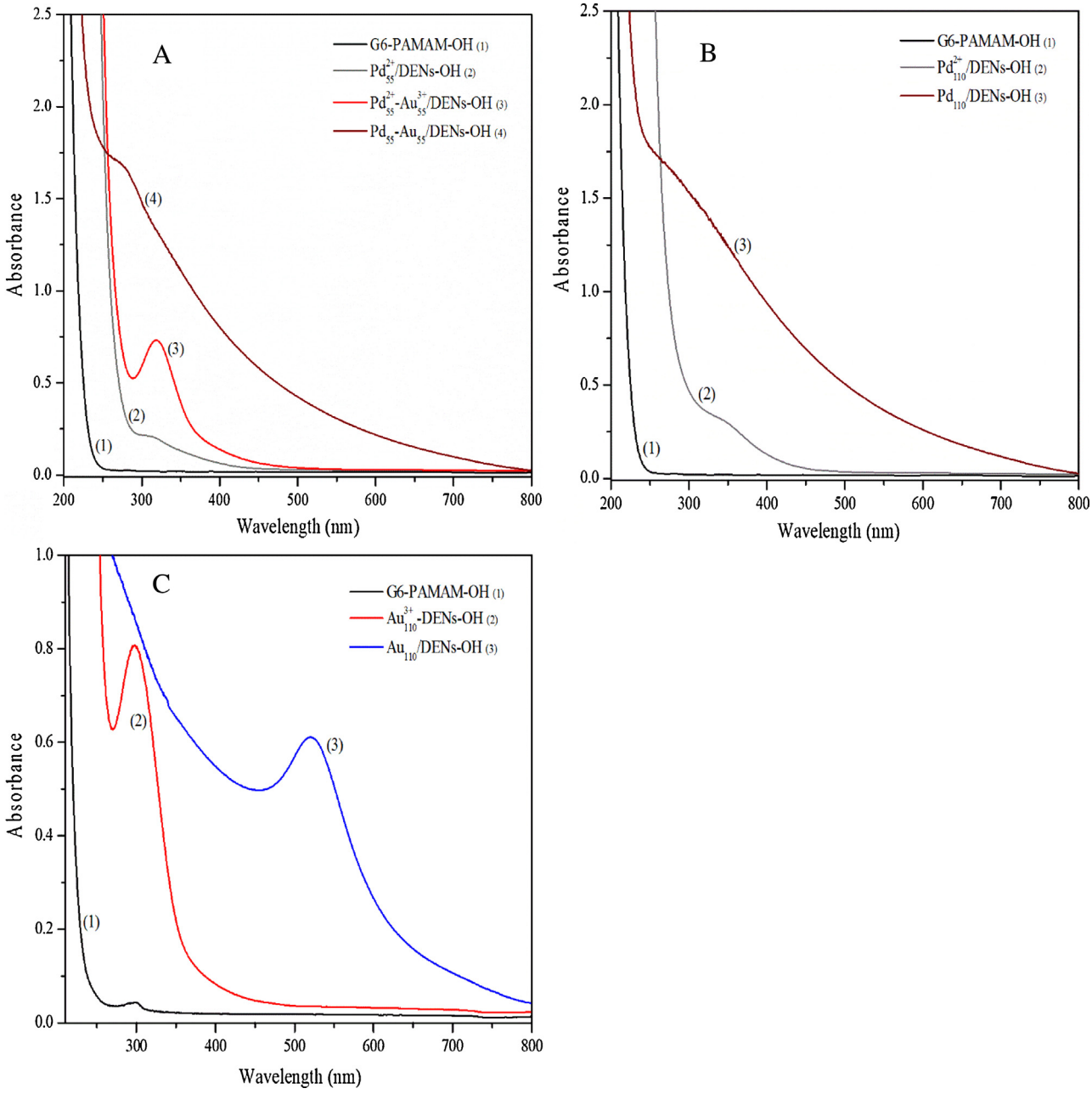

Fig. 1. (A), the UV–vis spectra of the encapsulated alloys nanoparticles synthesized at room temperature, and (B) and (C) show the synthesis of mono-metallic palladium and gold encapsulated, respectively.

transmission electron microscopy. The catalytic oxidation of morin as a benchmark reaction was used to evaluate the catalytic activity of the encapsulated random alloy nanoparticles in the presence of hydrogen peroxide. The activation energy related to the bi-metallic nanoparticles surface was interpreted following the Langmuir–Hinshelwood approach. Liquid chromatography analysis was performed in order to identify the product and to propose the oxidation mechanism.

2. Experimental

2.1. Materials and instruments

A 4.97 wt.% solution of methanol containing a sixth generation hydroxyl terminated poly(amido-amine) dendrimer was purchased from Dendritech®. The volatiles were removed *in vacuo* at room temperature. Chloroauric acid ($HAuCl_4 \times 3H_2O$, ≥99.9%), morin hydrate ($C_{13}H_{10}O_7 \times H_2O$, ≥98.0%), sodium borohydride ($NaBH_4$, ≥98.0%), 2,4-dihydroxybenzoic acid ($(OH)_2C_6H_3CO_2H$, ≥97.0%), and potassium tetrachloropalladate (K_2PdCl_4, ≥98.0%) were purchased from Sigma-Aldrich. Sodium hydroxide pellets (NaOH, ≥99.86%), and hydrogen peroxide 30% (H_2O_2, 30–35%) were obtained from Merck Laboratories. All the solutions were prepared using deionized water obtained from an in house Milli-Q system (18 MΩ cm) as a solvent. All the chemicals were used as received, without further purification.

To monitor the synthesis process of the encapsulated bi-metallic nanoparticles and the catalytic oxidation process of morin a Shimadzu UV-1800 spectrophotometer was used. Snakeskin® Dialysis Tubing (10 000 MWCO) purchased from Thermo-Scientific, was used to purify the colloidal alloy nanoparticle solutions. The encapsulated mono- and bi-metallic nanoparticle concentrations were

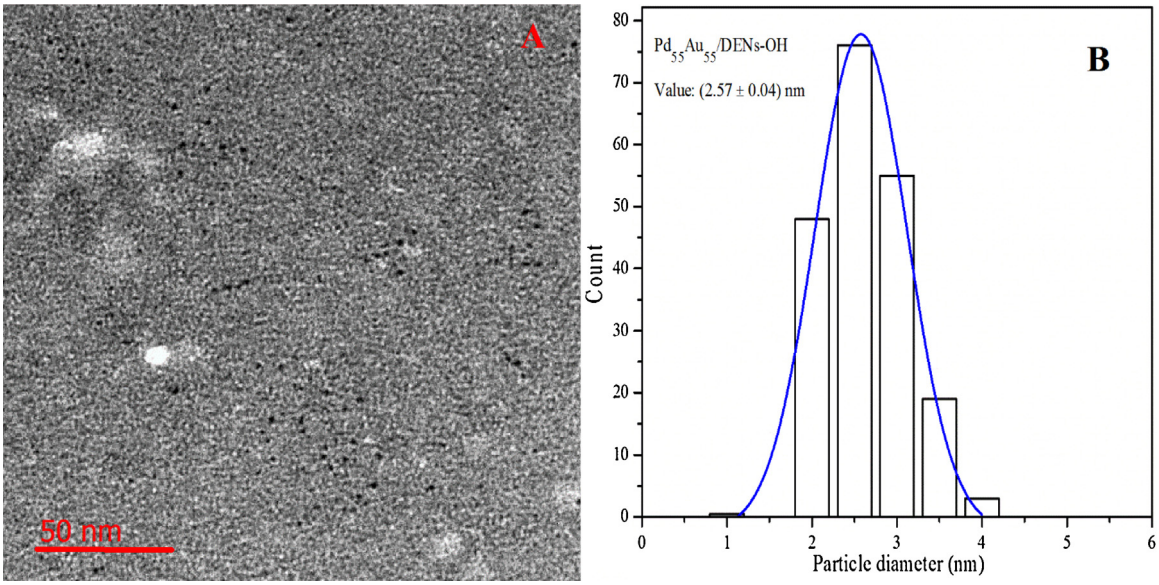

Fig. 2. TEM Micrograph of $Pd_{55}Au_{55}$/DENs-OH (A) and corresponding histogram of $Pd_{55}Au_{55}$/DENs-OH (B).

quantified based on the dendrimer concentration. The micrographs were obtained by high resolution transmission electron microscopy analysis performing on a JOEL JEM-2100F electron microscope with accelerating voltage of 200 kV using a copper grid. The average size of the random alloy nanoparticles was calculated using ImageJ software. The reaction intermediate was identified by a Shimadzu Ultra High Performance Liquid Chromatography (UHPLC) (Nexera Series (8030) Triple Quadrupole Instrument).

2.2. Synthesis

The synthesis of the encapsulated Pd_n-Au_{110-n} nanoparticles using a dendritic template was adapted from the literature [15,26,27]. The aqueous solution of 0.943×10^{-3} M chloropalladate (5×10^{-3} L, 0.471×10^{-3} mol) and 0.984×10^{-3} M chloroauric acid (5×10^{-3} L, 0.492×10^{-3} mol) were used as stock solutions, and an alkaline solution of 0.106 M sodium borohydride (1×10^{-3} L, 0.106×10^{-3} mol) was used as reducing agent stock. The series of random alloy (Pd_n-Au_{110-n}) nanoparticles were synthesized with n (molar ratio) equals to 0, 15, 35, 55, 75, 95, and 110. For each random alloy nanoparticle solutions prepared the concentration was 5×10^{-6} M and the volume 50×10^{-3} L. Palladium salt was added first to the aqueous dendrimer solution to assure the complexation with in the tertiary amine groups dendrimer and the solution was allowed to stir for an interval of 30–60 min. Approximately five minutes were provided to the gold salt for coordination to prevent their reduction by the hydroxyl groups located on the dendrimer surface. The formation of the random alloy nanoparticles was performed by chemical reduction through ten equivalent excess of sodium borohydride contained in sodium hydroxide solution ([NaOH] = 0.3 M). For the synthesis of encapsulated palladium nanoparticles, the reducing agent was prepared in aqueous solution. Table 1S shows the analytical detail of the synthesis approach in term of volume, and moles of reactants (see Supporting information). The purification of the random alloy nanoparticles was performed by dialysis against deionized water overnight to remove the excess of sodium borohydride. The encapsulated mono- or bimetallic nanoparticles were stable for over three months.

2.3. Catalytic oxidation of morin

To evaluate the catalytic performance of the encapsulated mono- and bi-metallic nanoparticles, morin oxidation was used as a model reaction. The oxidation process was monitored by UV–vis spectroscopy following the diminishing absorbance at λ 410 nm. In order to investigate the catalyst activity, the uncatalyzed reaction was performed as well. Exactly, 0.15×10^{-6} M of Pd_nAu_{110-n}/DENs-OH used as catalyst in the presence of 30×10^{-3} M of hydrogen peroxide to oxidize 0.1×10^{-3} M of morin, total volume of 3×10^{-3} L. The catalytic oxidation was performed at 25 °C. The oxidation of morin resulted in the formation of 2,4,6-trihydroxybenzoic acid and 2,4-dihydroxybenzoic acid which could undergo further decomposition [25].

The reaction pathway was proposed through a liquid chromatography analysis. An aqueous solution of 0.1×10^{-3} M morin and 30×10^{-3} M hydrogen peroxide at 50×10^{-3} L in a graduated Erlenmeyer flask was catalyzed by 0.15×10^{-6} M of $Pd_{55}Au_{55}$/DENs-OH contained in a dialysis bag. Exactly, 45 min was allocated to the reaction run prior to sample. A volume of 1.5×10^{-3} L of oxidized morin was filtrated to be analyzed.

2.4. Kinetic investigation

A major limitation in kinetic studies is the possibility of diffusion limitation in the process. Diffusion limitation occurs when the chemical reaction of the reactants is faster than their adsorption on the catalyst surface. The diffusion limitation can be ruled out by the use of the second Damköhler number (*DaII*) [28] express mathematically by Eq. (1).

$$DaII = \frac{k_{obs} \times [Morin]^{n-1}}{\beta \times \alpha} \quad (1)$$

where k_{obs} is the observed rate constant of reaction, [Morin] is morin concentration, n is the order of the reaction, β is the mass transfer coefficient and α is the total area of interface.

Theoretical bimolecular rate constant based on Fick's second law of diffusion [29,30] can also be considered to calculate the diffusion limitation zone. Fick's second law of diffusion is expressed mathematically in Eq. 1a (see Supporting information) which is

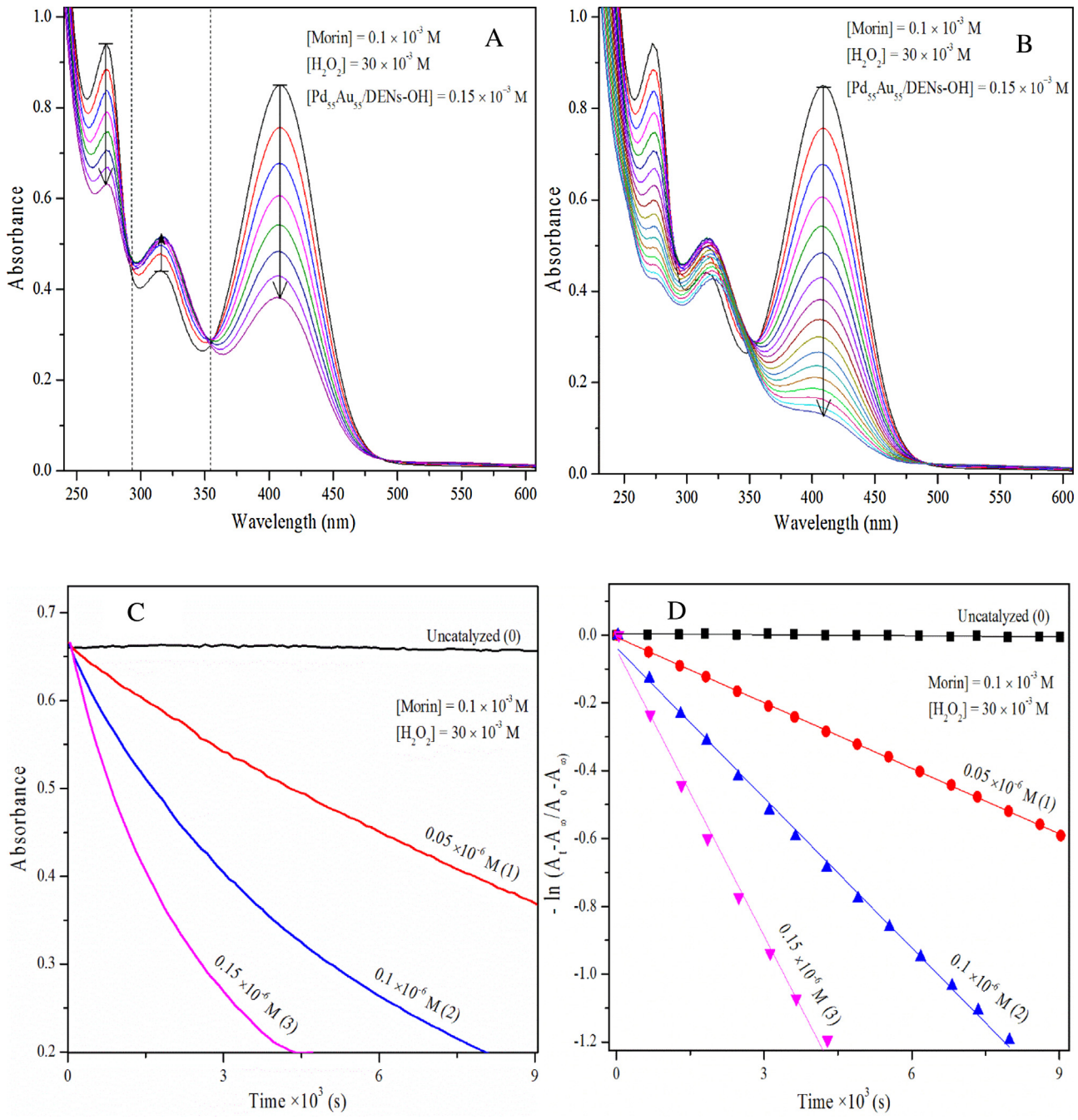

Fig. 3. Isosbestic point show in (A) highlighted the formation of products which oxidized further. (B) illustrated the oxidation process relate to morin concentration which present the center of interest in oxidation process. (C) and (D) show the kinetic process for the uncatalyzed process (0), and different concentrations (1)–(3) of $Pd_{55}Au_{55}$/DENs-OH.

reduced to Smoluchowski equation [30] considering that the diffusion term is significantly greater than the electron transport term. The Smoluchowski equation is given in Eq. (2).

$$k_{bm} = 4\pi rD \quad (2)$$

where k_{bm} is bimolecular rate constant, D is the diffusion coefficient of morin in aqueous phase, and r is the normalized rate constant.

The order of the catalytic oxidation process was determined to be *pseudo*-first order in morin considering that the concentration of the oxidizing agent was much larger than the other reactants [31–33]. The rate observed for the reaction was detected by monitoring the process with UV–vis spectroscopy. The decrease of adsorption at λ 410 nm relative to time was recorded. Considering that the concentration of hydrogen peroxide is taken in excess and the catalyst could be recovered. The kinetic *pseudo*-first order can be expressed mathematically by Eq. (3).

$$-\ln\frac{A_t - A_\infty}{A_0 - A_\infty} = k_{obs} \times t \quad (3)$$

The catalytic investigation was conducted using the Langmuir–Hinshelwood approach, which consist of the adsorption of the reactants on the catalyst surface as the rate-determining step of the reaction in order to form the active species [34,35]. In this approach, the catalyst surface consists of the uniform, and adjacent active sites. The reactants compete with each other to occupy the active sites and the most important factors in this

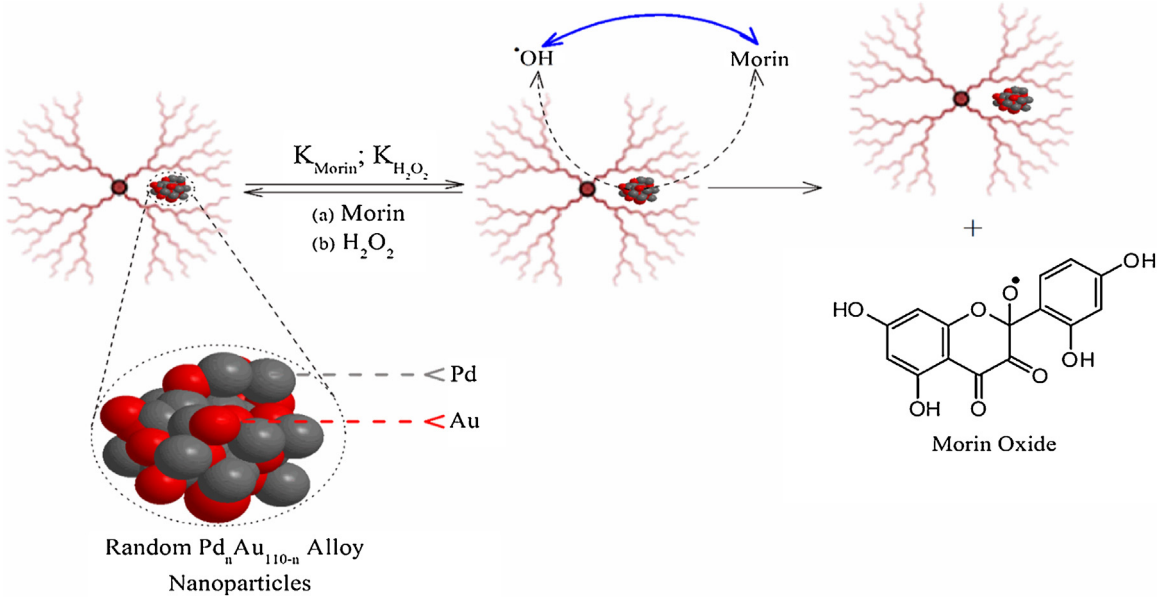

Fig. 4. The encapsulated bimetal nanoparticles used as catalyst in oxidation of morin by hydrogen peroxide.

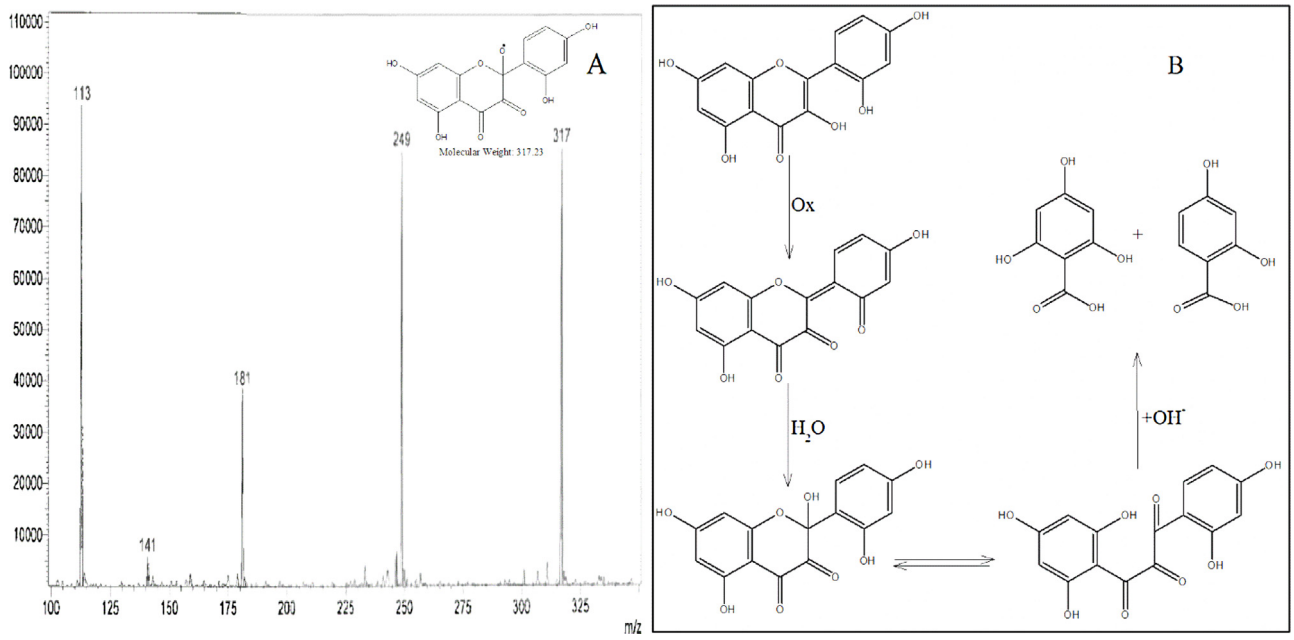

Fig. 5. Liquid chromatography spectrum of catalytic oxidation of morin by hydrogen peroxide (A), and the suggested morin oxidation pathway (B).

process are that an active site can be occupied by only one reactant and no interaction occurs with the adjacent sites. Experimentally, that can be evaluated by maintaining the concentration of morin constant while the concentration of hydrogen peroxide is varying, and inversely by keeping the hydrogen peroxide concentration constant, while the morin concentration will be varied. The kinetic analysis is mathematically derived in Supporting information. The catalytic process will be evaluated following the rate constant on the mono- and bi-metallic nanoparticles' surface, k, the normalized surface area, S, of the nanoparticles assuming that it described a spherical shape, and the concentration of morin ([Morin]) and hydrogen peroxide ($[H_2O_2]$), and equilibrium constant of morin (K_{Morin}) and hydrogen peroxide ($K_{H_2O_2}$). The observed rate constant from UV–vis spectroscopy, is expressed mathematically in the Eq. (4) [34].

$$k_{obs} = \frac{k \times S \times (K_{Morin})^n \times [Morin]^{n-1} \times \left(K_{H_2O_2} \times [H_2O_2]\right)^m}{\{1 + (K_{Morin} \times [Morin])^n + (K_{H_2O_2} \times [H_2O_2])^m\}^2} \quad (4)$$

The exponents n and m should not be confused with the reaction order, but describe the heterogeneity of the sorbent on the catalyst surface. Those exponent determine the type of adsorption isotherm, when n and m are equal to unity, this results in a the linear adsorption isotherm [36].

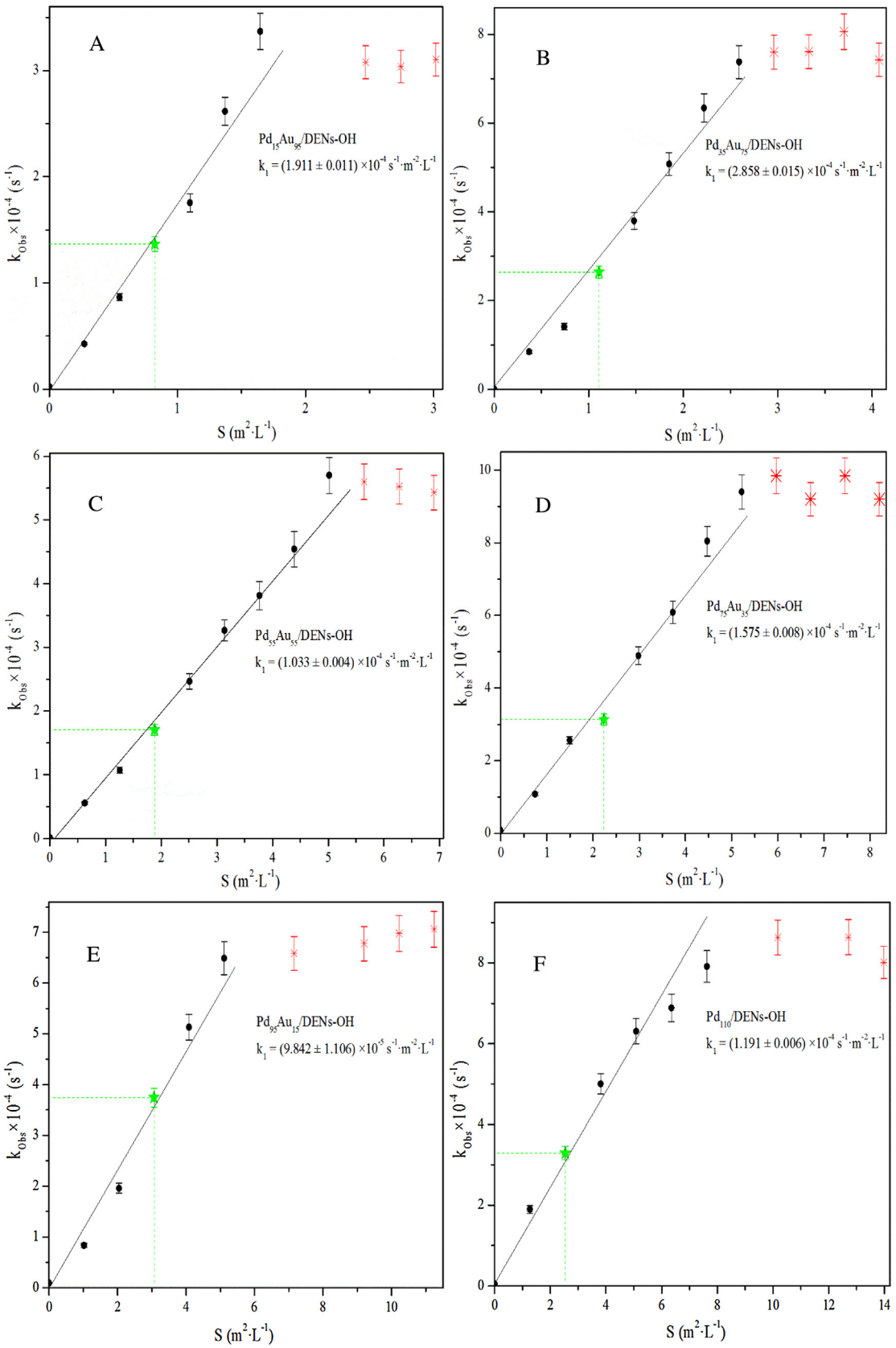

Fig. 6. A catalyst dependence of Pd_nAu_{110-n}/DENs-OH on morin oxidation by hydrogen peroxide performed at 15 °C. Diffusion limitation zone show with red points, and the catalyst normalized surface area used for the kinetic evaluation is indicated with a star point.(For interpretation of the references to color in this figure legend, the reader is referred to the web version of this article.)

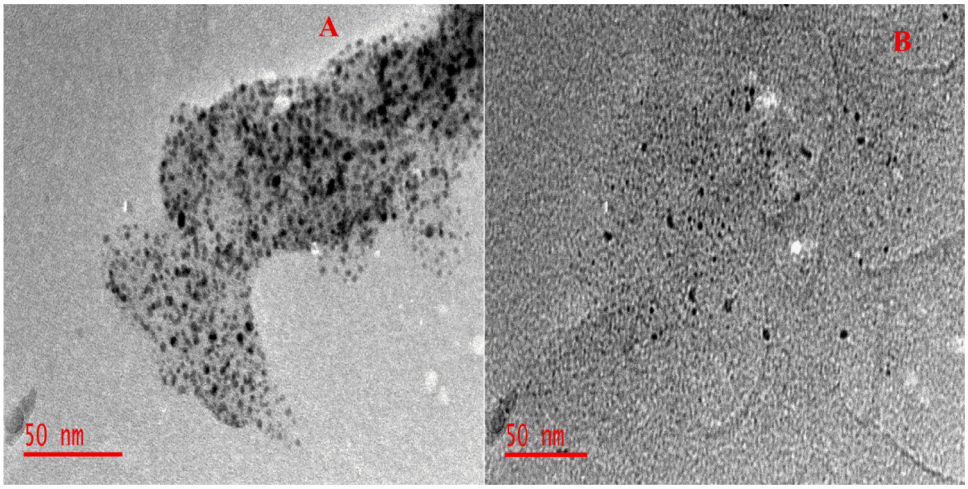

Fig. 7. Micrograph of $Pd_{55}Au_{55}$/DENs-OH (A) and Pd_{110}/DENs-OH (B) after reaction, showing the narrow dispersion of nanoparticles. Exactly, 0.1×10^{-3} M of morin was oxidized by 30×10^{-3} M of hydrogen peroxide in presence of 0.15×10^{-6} M of $Pd_{55}Au_{55}$/DENs-OH and Pd_{110}/DENs-OH, respectively.

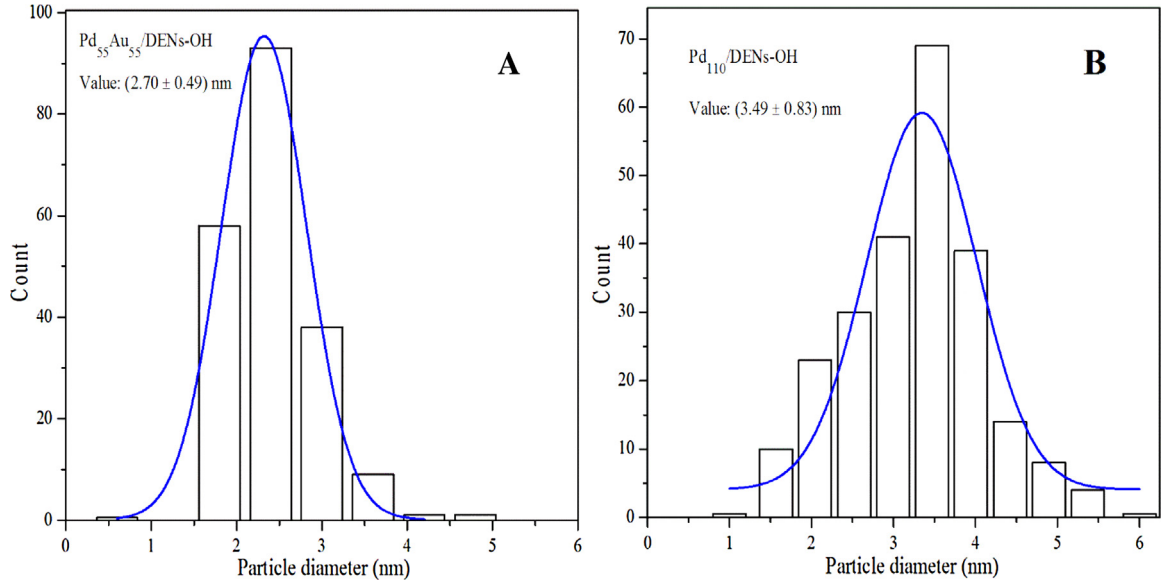

Fig. 8. The size distribution histograms of $Pd_{55}Au_{55}$/DENs-OH (A) and Pd_{110}/DENs-OH (B) after reaction.

3. Results and discussion

One of the advantages in synthesis of encapsulated nanoparticles using dendrimers is that the synthetic process can be monitored by UV–vis spectroscopy. The synthesis of alloy nanoparticles was performed following a co-complexation method which resulted in random metal nanoparticles [15]. The process was subdivided into five steps which are the aqueous dendrimer solution preparation (1), palladium ion coordination (2), gold ion coordination (3), alloy nanoparticle formation (4), and purification of the alloy nanoparticles (5). Fig. 1 shows the UV–vis spectra for each synthetic step of metal nanoparticle synthesis for the synthesis of $Pd_{55}Au_{55}$/DENs-OH, Pd_{110}/DENs-OH, and Au_{110}/DENs-OH. The peak detected in the λ 300–375 nm range (Fig. 1A (2)) is related to the complexation of dendrimer-palladium ions [37]. The addition of gold ions exhibited the maximum absorbance peak at λ 315 nm (Fig. 1A (3)). The ligand-to-metal charge transfer peak at λ 270 nm can be attributed to the formation of alloy nanoparticles [15]. In the synthesis of mono-gold nanoparticles, the maximum peak detected at λ 520 nm shows the gold nanoparticle formation [38].

The increase of catalytic activity at nano scale confirms the new method developed for their synthesis. A high resolution transmission electron microscopy analysis of Pd_nAu_{110-n}/DENs-OH was performed for each of the metal nanoparticles. A representative micrograph and histogram describing the size distribution for Pd55Au55 is given in Fig. 2. The micrographs of the metal nanoparticles, and their histograms for the other particles are presented in Supplementary information. The average size of the alloy nanoparticles was determined and those values were compared with the calculated size. The calculated particle sizes were determined by using Eq. (5), where, n is the total number of palladium and gold atoms, V_g is the average molar volume of both metals involved, and R represents the particle radius [37,39]. Table 1 shows the average calculated and the obtained size of the nanoparticles.

$$n = \frac{4 \times \pi \times R^3}{3 \times V_g} \quad (5)$$

Two isosbestic points were identified after 30 min of monitoring the catalytic process, indicating that one product is formed (Fig. 3A). The relative decrease of the absorbance at λ 410 nm is directly

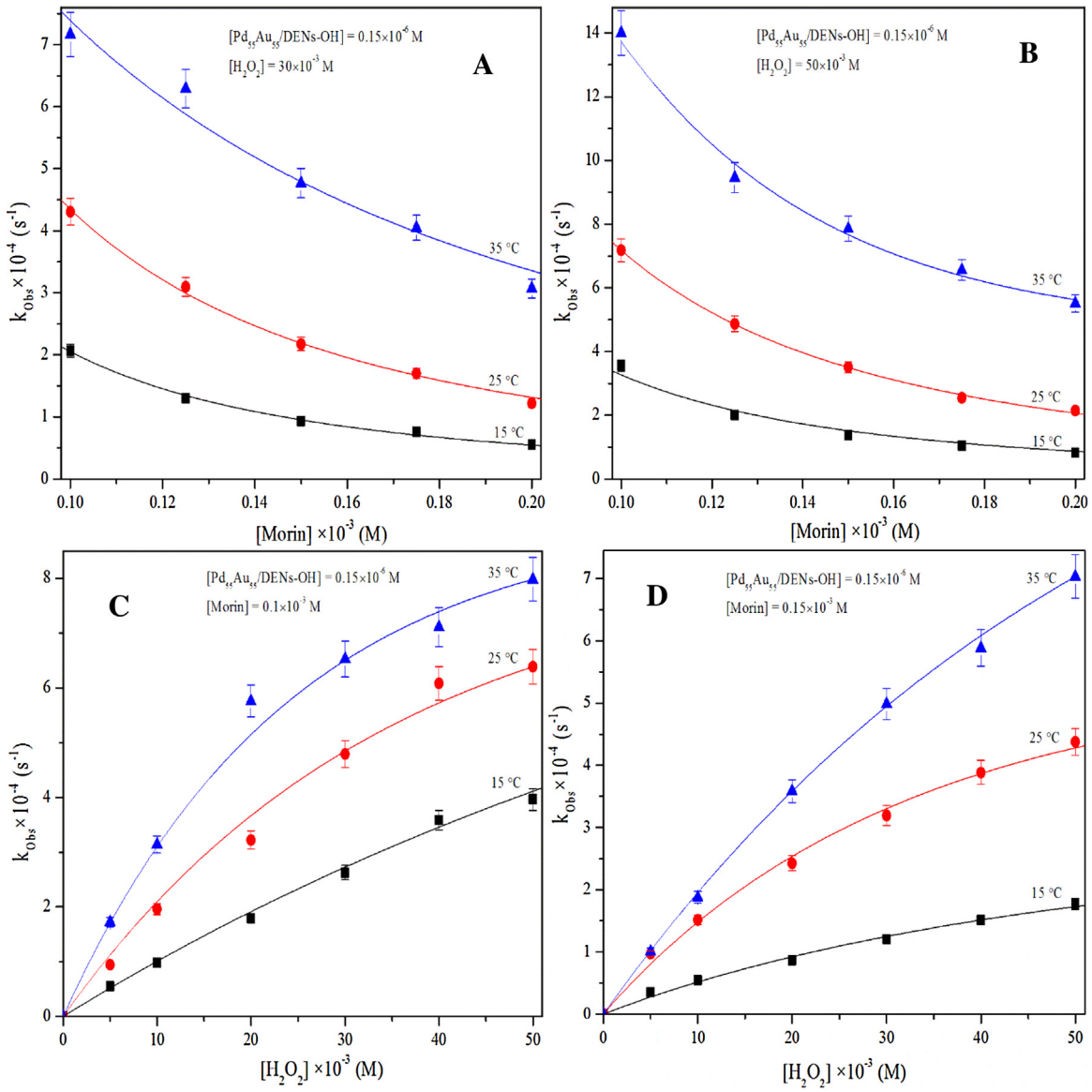

Fig. 9. Dependency of observed rate constant, $k_{obs,}$ on the concentration of morin keeping hydrogen peroxide concentration constant (30×10^{-3} M (A), 50×10^{-3} M (B)), and the hydrogen peroxide concentration maintaining the morin concentration constant (0.1×10^{-3} M (C), 0.15×10^{-3} M (D)). The lines show the best fitted through Langmuir-Hinshelwood approach.

Table 1
Average particle sizes determined and calculated.

Average particle diameters × 10^{-9} (m)		
Catalyst	Calculated	Determined
Au_{110}/DENs-OH	2.83	2.63 ± 0.58
$Pd_{15}Au_{95}$/DENs-OH	2.77	2.38 ± 0.55
$Pd_{35}Au_{75}$/DENs-OH	2.68	2.49 ± 0.46
$Pd_{55}Au_{55}$/DENs-OH	2.59	2.57 ± 0.34
$Pd_{75}Au_{35}$/DENs-OH	2.49	3.03 ± 0.53
$Pd_{95}Au_{15}$/DENs-OH	2.39	3.49 ± 0.67
Pd_{110}/DENs-OH	2.31	3.67 ± 0.23

related to the decrease of morin concentration. The kinetics of the reaction could be accurately measured at λ 410 nm. The monitoring of catalytic oxidation process is illustrated in Fig. 3B. The formation of byproducts and their further decomposition are not the focus of our studies, thus, the catalytic oxidation of morin can be monitored at λ 410 nm. To investigate if molecular oxygen its interfering while the catalytic oxidation of morin was performed, molecular oxygen from an air pump was used as oxidizing agent to oxidize morin in presence of a set amount of catalyst (see Supporting information, Fig. 1S). The interference of oxygen in the catalytic process can be ruled out by the fact that the morin absorbance spectrum remains stable over the reaction time. The relative adsorption as the function of reaction time is shown in Fig. 3C, which demonstrates the catalytic activity of alloy nanoparticles compared to the uncatalyzed process. The catalytic oxidation of morin takes place immediately after adding the nanoparticles and a normalized adsorption shows a linear decrease. That described the *pseudo*-first order according to Eq. (3). Fig. 3D shows the reaction order plot of the uncatalyzed and the catalyzed process. The catalytic dissociation of hydrogen peroxide to produce the hydroxyl radical which oxidized the morin does not take place without the alloy nanoparticles [40]. Recently, we published the synthesis of dendrimer templated gold nanoparticles, and their catalytic activity was evaluated using morin oxidation as model reaction [35]. In this work, a carbonate buffer was used as pH stabilizer, and also to facilitate the adsorption of morin on the catalyst surface. Here,

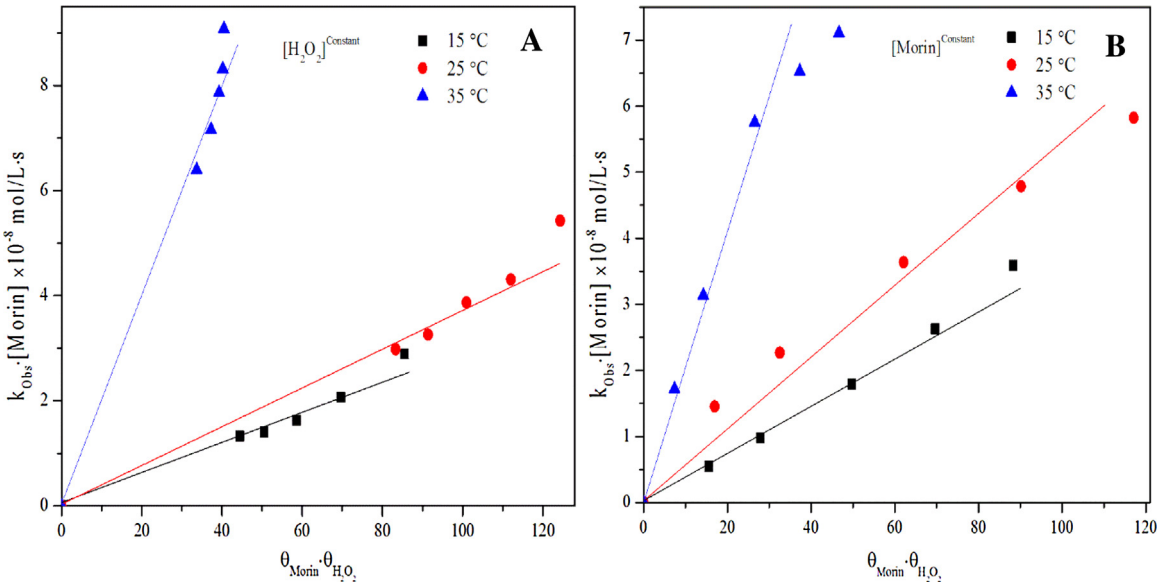

Fig. 10. The validity of fitted data according Langmuir-Hinshelwood maintaining constant hydrogen peroxide concentration constant (A), and morin concentration constant (B) considering $Pd_{55}Au_{55}$/DENs-OH.

no buffer solutions were applied and consequently the encapsulated gold nanoparticles did not show any catalytic activity (Fig. 2S, see Supporting information).

The reaction pathway was suggested using an ultra-high performance liquid chromatography analysis which confirms the presence of oxidized morin. The assumption of the catalytic oxidation of morin is displayed in Fig. 4. Colombini and coworkers reported that this molecule undergoes a decomposition which results in the formation of two benzoic acids [25]. Those benzoic acids can be decarboxylated. Fig. 5 describes the liquid chromatography spectrum (A), and the suggested oxidation pathway (B).

To evaluate the catalyst activity, the catalytic process was investigated by keeping all reactant concentrations constant while the catalyst amount is increased. The evaluation was performed at 15 °C with concentration of 0.1×10^{-3} M of morin, and 30×10^{-3} M of hydrogen peroxide, in a total volume of 3×10^{-3} L. The rate-determining step of the catalytic process consists of adsorption of the reactants on the catalyst actives sites prior to the reaction [41,42]. The correlation of catalytic activity exhibited by nanoparticles with their size were reported in literature [43,44]. Those reports presented a contrasting correlation between nanoparticle activity and their size. Based on those reports, the nanoparticle size does not describe a unique parameter which describes the catalytic activity demonstrated by nanoparticles. The surface normalized rate constant, k_1, was determined by constructing the plot of observed rate constant, k_{obs}, versus the volume normalized surface area of nanoparticles following Eq. (6). That describe a linear relationship, where the slope is the surface normalized rate constant. This was expected but the fact that the observed rate should increase with the large catalyst surface area. Fig. 6 shows the plots of observed rate constant versus a volume normalized surface area of each alloy nanoparticle involved. The surface normalized rate constant determined for each catalyst used are: $(1.91 \pm 0.1) \times 10^{-4}$ ($Pd_{15}Au_{95}$/DENs-OH), $(2.86 \pm 0.01) \times 10^{-4}$ ($Pd_{35}Au_{75}$/DENs-OH), $(1.03 \pm 0.00) \times 10^{-4}$ ($Pd_{55}Au_{55}$/DENs-OH), $(1.57 \pm 0.01) \times 10^{-4}$ ($Pd_{75}Au_{35}$/DENs-OH), $(9.84 \pm 1.11) \times 10^{-5}$ ($Pd_{95}Au_{15}$/DENs-OH), and $(1.19 \pm 0.01) \times 10^{-4}$ (Pd_{110}/DENs-OH) $s^{-1}\,m^{-2}\,L^{-1}$.

The red zone shown in Fig. 6 demonstrats the diffusion limitation zone where the chemical reaction of reactants is faster than their adsorption on the catalyst surface. The second Damköhler number (*DaII*) is defined by the chemical reaction rate over a diffusion mass transport of the reactants, was applied to calculate diffusion limitation during catalytic performance [28].

$$k_{obs} = k_1 \times S \tag{6}$$

The second Damköhler number expressed mathematically by Eq. (1) was applied to determine the diffusion zone. To estimate the mass transfer coefficient, β, the diffusion coefficient of morin which is equal to 5.45×10^{-10} m^2/s [24] was divided by the sixth generation hydroxyl terminated PAMAM dendrimer diameter ($\delta = 6.7 \times 10^{-9}$) [1]. The observed rate constant considered for each alloy nanoparticle while the kinetic investigation is illustrated with a green star in Fig. 6. The total area interface, ɑ, was deduced from the determined average diameter for each of the nanoparticles. The oxidizing agent was used in large excess, which resulted in a *pseudo*-first order reaction (n = 1). The estimated values of *DaII* were far below unity. That demonstrated that the catalytic oxidation of morin performed in kinetic domain. Table 2 shows the calculated values of *DaII*, and the total area interface. Additionally, Fick's second law of diffusion was applied to rule out the diffusion-controlled zone during the catalytic process. Assuming that the diffusion of the reactant is significantly fast Fick's equation is reduced to the Smoluchowski equation (Eq. (2)). The bimolecular rate constant was determined from the slope of k_{obs} versus volume normalized of surface area for each alloy nanoparticle, as well the mono-metallic nanoparticles. The calculated values are reported in Table 2, and are orders of magnitude below unity. Therefore, diffusion limitation is negligible under the conditions applied for the kinetic investigation.A micrograph was recorded of the catalyst after the reaction, to investigate if the nanoparticles remained stable. The metal nanoparticles show a narrow dispersion, which confirm their stability while the catalytic oxidation process. The determined average diameter of $Pd_{55}Au_{55}$/DENs-OH, and Pd_{110}/DENs-OH after catalytic process are 2.70 ± 0.49 nm and 3.49 ± 0.83 nm, respectively. The nanoparticles average diameter after reaction are slightly different compared to their average diameter before reaction. The micrograph and the nanoparticles size distribution are shown in Figs. 7 nad 8, respectively.

The catalytic activity of the alloy nanoparticles was investigated following the Langmuir–Hinshelwood approach, due to the lack of evidence to relate the catalytic activity to the nanoparticles size. The

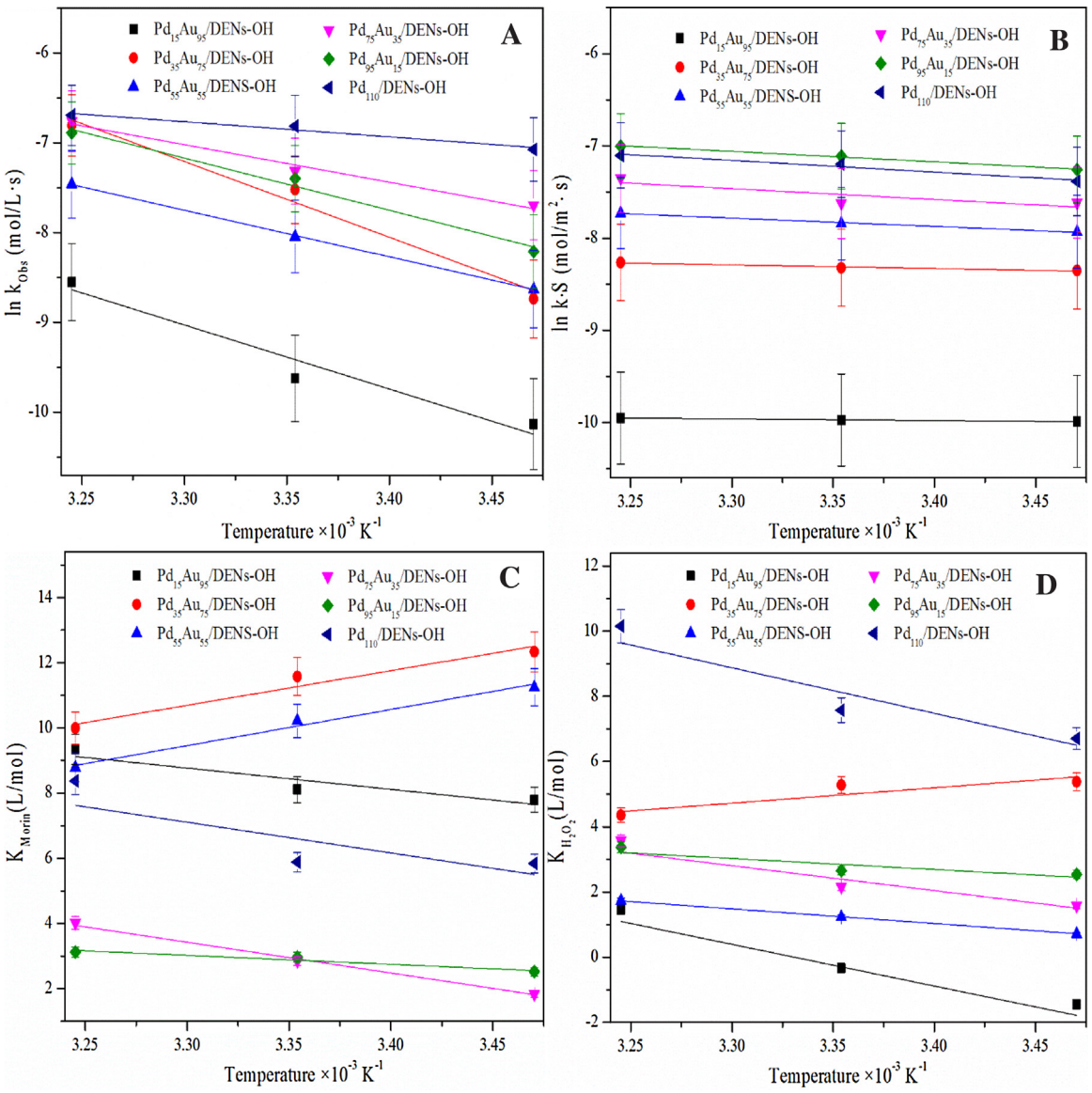

Fig. 11. The dependency of observed rate constant, and kinetic rate constant on the temperature present at (A) and (B), respectively. The temperature influence on the adsorption equilibrium constant of morin (C) and hydrogen peroxide (D).

Table 2
A calculated value of *DaII*, total area interface, and mass transfer coefficient for each catalyst.

Catalyst	$k_{obs} \times 10^{-4}$ (s^{-1})	β ($m\,s^{-1}$)	α (m^{-1})	*DaII* × 10^{-6}	$k_{bm} \times 10^{-6}$ ($m^{-1}\,s^{-1}$)
Au_{110}/DENs-OH	Unreacted	0.081	1963.15	Unknown	Unknown
$Pd_{15}Au_{95}$/DENs-OH	1.37		1607.66	0.82	6.54
$Pd_{35}Au_{75}$/DENs-OH	2.64		1759.71	1.85	9.79
$Pd_{55}Au_{55}$/DENs-OH	1.70		1874.59	1.12	3.53
$Pd_{75}Au_{35}$/DENs-OH	3.14		2605.71	1.48	5.37
$Pd_{95}Au_{15}$/DENs-OH	3.74		3456.94	1.33	3.37
Pd_{110}/DENs-OH	3.29		2548.48	1.59	4.07

adsorption approach developed by Langmuir–Hinshelwood considers a catalyst as a surface composed of the equal and uniform active sites. Assuming that those active sites can only be occupied by one substrate. In the presence of two or more substrates this will lead to the competitive adsorption on the catalyst surface [18,35]. The catalytic oxidation of morin by hydrogen peroxide was kinetically evaluated at different temperatures according to the Langmuir view. A morin concentration ranging from 0.1×10^{-3} M to 0.2×10^{-3} M was used to evaluate adsorption while the hydrogen peroxide concentration was kept constant. Inversely, the morin concentration was maintained constant while hydrogen peroxide concentration was varied. A range of $10–50 \times 10^{-3}$ M hydrogen peroxide was considered to investigate the adsorption process. Three different temperatures which are 15 °C, 25 °C, and 35 °C were considered to examine the temperature involvement during the adsorption process. For the reliability of the kinetic investigation all the processes were performed using the same stock of catalyst.

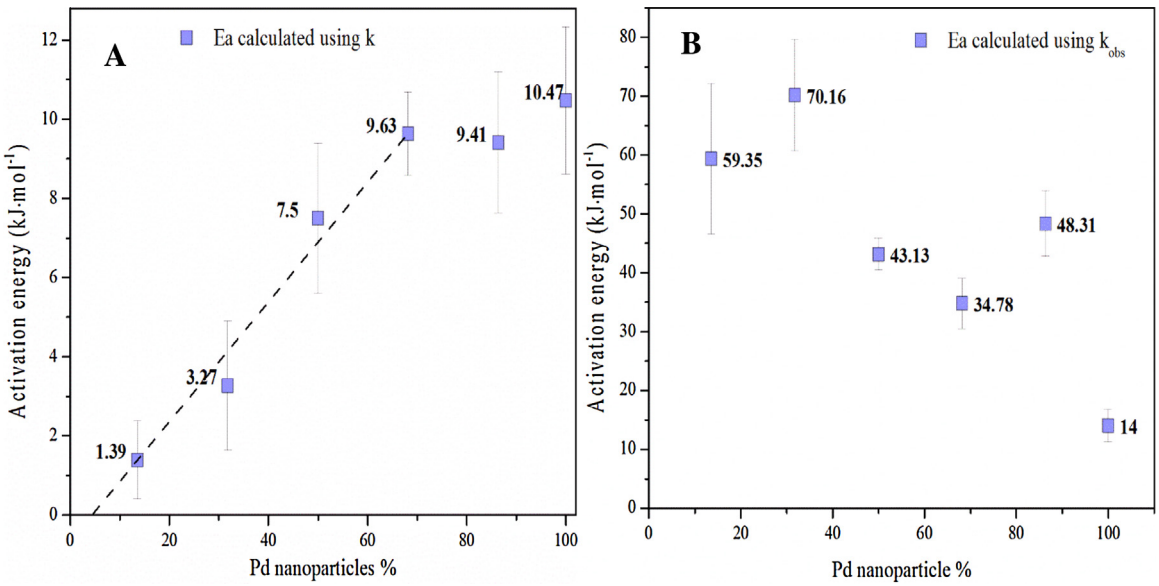

Fig. 12. Activation energy versus Pd nanoparticle mole percentage used in alloy nanoparticle preparation. The activation energy on the catalyst surface (A), and the catalytic oxidation process (B).

The adsorption process of hydrogen peroxide onto a catalyst surface is a complex reaction which requires additional analysis. We assume that the hydrogen peroxide adsorption leads to a formation of a hydroxyl radical, a high potential oxidant, which will oxidize morin [40]. A great consideration in the use of morin as model compound to evaluate the metal nanoparticles catalytic activities consist in their ability to remain a monomer during the oxidation process [25].

An observed rate constant as a function of morin or hydrogen peroxide concentration is shown in Fig. 9 related to $Pd_{55}Au_{55}$/DENs-OH, for the remaining bimetallic nanoparticles and palladium nanoparticles see Supporting information (Fig. S5). The increase of morin amount while hydrogen peroxide concentration is kept constant results in a decrease of the observed rate constant. That highlighted the fact that most of the active sites are occupied by morin. Therefore, the formation of hydroxyl radical is significantly decreased. Oppositely, increasing the hydrogen peroxide amount will directly increase the hydroxyl radicals as long that morin amount was kept constant. High presence of hydroxyl radicals has a consequence the enhancing of observed rate constant.

To evaluate the reliability of Langmuir–Hinshelwood mechanism, the data were fitted using Eley–Rideal mechanism [45] and Mars–Van Krevelen mechanism [46]. The observed rate constant related to Eley–Rideal mechanism results in a rate independence of one reactant (morin in this case). Mars–Van Krevelen mechanism consist on adsorption the oxygen atom onto the catalyst surface leading to the formation of oxidizing species. Considering the small size of the encapsulated alloy nanoparticles, the storage of oxygen inside the dendrimer structure would not be considerable. The kinetic data of $Pd_{55}Au_{55}$/DENs-OH were fitted using Eley–Rideal and Mars–Van Krevelen mechanism, respectively (see Supporting information, Fig. S6 and Fig. S7).

The observed rate constant versus morin or hydrogen peroxide concentration data would be kinetically evaluated through Langmuir–Hinshelwood approach. The obtained data was fitted using Eq. (4). The outcome of the fitting is reported in Table 3, showing the kinetic rate related on the catalyst surface. The equilibrium constant of morin and hydrogen peroxide were also determined and the value show as well in Table 3. The validity of the fitting data performed through Langmuir–Hinshelwood approach was evaluated plotting the plot $k_{obs} \times$ [Morin] versus the product of $\theta_{Morin} \times \theta_{H_2O_2}$ according Eq. (6). A slope is the product of kinetic rate constant and normalized surface area. The slope describes the error propagation through the calculation of θ_{Morin} and $\theta_{H_2O_2}$, respectively. Fig. 10 show the fitting data validity for $Pd_{55}Au_{55}$/DENs-OH.

$$k_{obs} \times [Morin] = k \times S \times \theta_{Morin} \times \theta_{H_2O_2} \quad (6)$$

The Arrhenius equation was used to determine the activation energy related to the catalyst surface by establishing the linear relationship of kinetic rate constant, k, on the catalyst surface and the temperature [47]. The observed rate constant versus temperature plot was also constructed to obtain the activation energy relative to the oxidation process. The Fig. 11A–B show the Arrhenius plot related to the kinetic rate constant onto the catalyst surface and observed rate constant, respectively. The thermodynamic parameters referring to the catalytic oxidation process and on the catalyst surface were investigated using the Eyring equation [48]. The adsorption process onto the catalyst surface can be described in terms of enthalpy and entropy of activation. The enthalpy and entropy of activation for the reactants involved, morin and hydrogen peroxide, were obtained through Van's Hoff's equation. The dependency of the equilibrium constant of both reactants on the temperature is shown in Fig. 11C–D for morin and hydrogen peroxide, respectively. The activation energy related to the catalyst surface and the catalytic oxidation process, and the thermodynamic parameters of both reactants as well on the catalyst surface and the reaction are shown in Table 4.

The activation energy calculated using the observed rate constant describe a higher value compared to the activation energy calculated through the kinetic rate constant. This observation can be explained by the relativity of the observed rate constant on the kinetic rate constant, and adsorption constant of the reactants. The kinetic activity on the alloy nanoparticle surface increase proportionally with the relative amount of palladium. However, at 65% of palladium no significant increase was observed in term of kinetic activity. The plots of percentage palladium in the nanoparticles versus the activation energy calculated using kinetic rate constant and observed rate constant are shown in Fig. 12A–B. The adsorption process of morin and hydrogen peroxide on alloy nanoparticles surface are a spontaneous process. However, the hydrogen peroxide adsorption on $Pd_{15}Au_{95}$/DENs-OH is a non-spontaneous process. The thermodynamic parameters values are shown at Table 4.

Table 3
Experimental data obtained according Langmuir-Hinshelwood approach fitted for Pd_nAu_{110-n}/DENs-OH at different temperatures.

$Pd_{15}Au_{95}$/DENs-OH

T. (°C)	k ($\times10^{-5}$ mol/Ls)	K_{Morin} ($\times10^{+3}$ L/mol)	K_{H2O2} (L/mol)	n	m
15	5.58 ± 2.17	2.42 ± 1.38	0.23 ± 0.15	1.00 ± 0.00	0.95 ± 0.04
25	5.66 ± 2.22	3.32 ± 1.43	0.71 ± 0.34	1.00 ± 0.02	0.99 ± 0.01
35	5.78 ± 1.76	11.34 ± 1.30	4.29 ± 2.69	1.00 ± 0.01	0.97 ± 0.03

$Pd_{35}Au_{75}$/DENs-OH

T. (°C)	k ($\times10^{-4}$ mol/Ls)	K_{Morin} ($\times10^{+5}$ L/mol)	K_{H2O2} ($\times10^{+2}$ L/mol)	n	m
15	2.13 ± 0.22	2.28 ± 0.39	2.17 ± 0.37	1.00 ± 0.00	0.89 ± 0.05
25	2.19 ± 0.24	1.07 ± 0.18	1.97 ± 0.33	1.00 ± 0.02	0.96 ± 0.03
35	2.32 ± 0.28	0.22 ± 0.06	0.78 ± 0.13	1.00 ± 0.01	0.96± 0.04

$Pd_{55}Au_{55}$/DENs-OH

T. (°C)	k ($\times10^{-4}$ mol/Ls)	K_{Morin} ($\times10^{+4}$ L/mol)	K_{H2O2} (L/mol)	n	m
15	1.91 ± 1.31	7.67 ± 5.67	2.05 ± 1.19	1.00 ± 0.00	0.85 ± 0.20
25	2.09 ± 1.38	2.75 ± 1.84	3.43 ± 1.47	1.00 ± 0.00	0.95 ± 0.04
35	2.34 ± 1.47	6.54 ± 4.04	5.66 ± 3.68	1.00 ± 0.00	0.99 ± 0.01

$Pd_{75}Au_{35}$/DENs-OH

T. (°C)	k ($\times10^{-4}$ mol/Ls)	K_{Morin} (L/mol)	K_{H2O2} (L/mol)	n	m
15	1.92 ± 0.01	6.23 ± 2.05	4.79 ± 2.38	1.00 ± 0.00	0.95 ± 0.05
25	2.19 ± 0.12	17.18 ± 2.85	8.60 ± 3.44	1.00 ± 0.02	0.95 ± 0.05
35	2.87 ± 0.87	55.39 ± 5.87	35.51 ± 3.42	1.00 ± 0.01	1.00± 0.01

$Pd_{95}Au_{15}$/DENs-OH

T. (°C)	k ($\times10^{-4}$ mol/Ls)	K_{Morin} (L/mol)	K_{H2O2} (L/mol)	n	m
15	2.30 ± 0.80	12.44 ± 1.42	12.66 ± 1.78	1.00 ± 0.00	0.93 ± 0.04
25	2.66 ± 0.50	19.38 ± 1.08	14.19 ± 1.81	1.00 ± 0.00	0.93 ± 0.04
35	2.97 ± 0.21	22.65 ± 1.79	29.21 ± 3.45	1.00 ± 0.00	0.97 ± 0.03

Pd_{110}/DENs-OH

T. (°C)	k ($\times10^{-4}$ mol/Ls)	K_{Morin} ($\times10^{+2}$ L/mol)	K_{H2O2} ($\times10^{+2}$ L/mol)	n	m
15	2.44 ± 0.86	3.44 ± 0.32	8.20 ± 1.25	1.00 ± 0.00	0.93 ± 0.04
25	2.95 ± 0.75	3.59 ± 0.55	19.50 ± 3.07	1.00 ± 0.01	0.95 ± 0.04
35	3.32 ± 0.53	43.20 ± 6.66	256.46 ± 38.24	1.00 ± 0.01	0.97 ± 0.03

Table 4
Activation energy of the catalytic oxidation process on the catalyst surface, and the thermodynamic parameters related to the reactants, and the catalyst surface.

Pd_nAu_{110-n}/DENs-OH	Parameters	Ea (kJ mol^{-1})	$\Delta H^{\#}$ (kJ mol^{-1})	$\Delta S^{\#}$ (J mol^{-1})	$\Delta G^{\#}$[a] (kJ mol−1)
$Pd_{15}Au_{95}$	k_{obs} (mol/Ls)	59.35 ± 12.81	55.64 ± 13.03	−85.61 ± 75.96	−80.29
	k (mol/Ls)	1.39 ± 0.98	−1.08 ± 0.11		
	K_{Morin} (L/mol)		54.33 ± 21.12	252.18 ± 71.18	−18.34
	K_{H2O2} (L/mol)		106 ± 27.09	354.22 ± 90.91	4.28
$Pd_{35}Au_{75}$	k_{obs} (mol/Ls)	70.16 ± 9.45	69.06 ± 9.27	−82.83 ± 80.34	−92.92
	k (mol/Ls)	3.27 ± 1.63	0.79 ± 0.66		
	K_{Morin} (L/mol)		−88.36 ± 18.84	−202.69 ± 62.97	−29.96
	K_{H2O2} (L/mol)		−39.27 ± 17.33	−90.30 ± 57.91	−13.25
$Pd_{55}Au_{55}$	k_{obs} (mol/Lns)	43.13 ± 0.72	40.60 ± 0.69	−89.75 ± 58.91	−66.44
	k (mol/Ls)	7.50 ± 3.63	5.02 ± 0.69		
	K_{Morin} (L/mol)		−92.13 ± 10.34	−225.39 ± 34.53	−27.18
	K_{H2O2} (L/mol)		37.27 ± 0.39	135.31 ± 1.36	−1.72
$Pd_{75}Au_{35}$	k_{obs} (mol/Ls)	34.78 ± 4.35	31.98 ± 4.35	−106.62 ± 91.42	−62.69
	k (mol/Ls)	9.63 ± 0.28	7.15 ± 6.10		
	K_{Morin} (L/mol)		78.48 ± 4.68	287.47 ± 15.96	−4.35
	K_{H2O2} (L/mol)		63.46 ± 19.48	232.77 ± 66.43	−3.61
$Pd_{95}Au_{15}$	k_{obs} (mol/Ls)	48.31 ± 5.59	46.40 ± 5.54	−86.75 ± 74.52	−71.39
	k (mol/Ls)	9.41 ± 1.79	6.93 ± 0.61		
	K_{Morin} (L/mol)		22.89 ± 5.47	100.65 ± 18.44	−6.12
	K_{H2O2} (L/mol)		28.04 ± 14.30	117.72 ± 48.30	−5.88
Pd_{110}	k_{obs} (mol/Ls)	14.00 ± 2.75	11.61 ± 2.75		
	k (mol/Ls)	10.47 ± 1.86	8.03 ± 1.88		
	K_{Morin} (L/mol)		78.41 ± 58.97	317.84 ± 199.39	−8.42
	K_{H2O2} (L/mol)		115.95 ± 40.48	456 ± 139.56	−2.37

[a] At 0.1 mM Morin and 30 mM H_2O_2 (15 °C).

4. Conclusion

The catalytic activity of a series of palladium and gold alloy nanoparticles was investigated through the oxidation of morin by hydrogen peroxide as a model reaction. A full kinetic investigation related to the catalytic oxidation process and the alloy nanoparticle surfaces were realized, and the results were analyzed according to the Langmuir–Hinshelwood mechanism. A sixth generation hydroxyl terminated PAMAM dendrimer was used as a template in alloy nanoparticle synthesis. That provide a stability and the accessibility of alloy nanoparticles while the catalytic process. The adsorption of the reactant on the catalyst surface consist the rate-determining step on catalytic process. Langmuir–Hinshelwood approach clarified the adsorption process of the morin and hydrogen peroxide on the catalyst surface. The clarification of the adsorption process is explained by determining the kinetic constant on the catalysts surface, and thermodynamic adsorption constants of morin and hydrogen peroxide. The catalytic activity described by alloy nanoparticles increase proportionally with the amount of palladium nanoparticles. However, no significant increase was observed at 65% of amount of palladium nanoparticles.

Appendix A. Supplementary data

Supplementary data associated with this article can be found, in the online version, at http://dx.doi.org/10.1016/j.apcatb.2016.02.040.

References

[1] Y. Niu, R.M. Crooks, Catal. Rev. 6 (2003) 1049–1059.
[2] D.A. Tomalia, L. Balogh, J. Am. Chem. Soc. 120 (1998) 7355–7356.
[3] M.Q. Zhao, L. Sun, R.M. Crooks, J. Am. Chem. Soc. 120 (1998) 4877–4878.
[4] U. Boas, J.B. Christensen, P.M.H. Heegaard, J. Mater. Chem. 16 (2006) 3785–3798.
[5] J. Kassube, L. Gade, Stereoselective dendrimer catalysis, in: L. Gade (Ed.), Dendrimer Catalysis, Springer, Berlin Heidelber, 2006, pp. 61–96.
[6] Y. Niu, R.M. Crooks, C. R. Chim. 6 (2003) 1049–1059.
[7] O. Paillai, R. Panchagnula, Curr. Opin. Chem. Biol. 5 (2001) 447–451.
[8] K. Tejaswini, V. Kadam, K. Dhanavade, V. Salunkhe, J. Pharm. Pharmacol. 2 (2013) 4815–4830.
[9] Z. Sideratou, D. Tsiourvas, C.M. Paleos, Langmuir 16 (2000) 1766–1769.
[10] D. Astruc, F. Lu, J.R. Aranzaes, Angew. Chem. Int. Ed. 44 (2005) 7852–7872.
[11] R. Nakao, H. Rhee, Y. Uozumi, Org. Lett. 7 (2005) 163–165.
[12] C. Burda, X. Chen, R. Narayanan, M.A. El-Sayed, Chem. Rev. 105 (2005) 1025–1102.
[13] M. Zhao, L. Sun, R.M. Crooks, J. Am. Chem. Soc. 120 (1998) 4877–4878.
[14] H. Lang, S. Maldonado, K.J. Stevenson, B.D. Chandler, J. Am. Chem. Soc. 126 (2004) 12949–12956.
[15] M.G. Weir, M.R. Knecht, A.I. Frenkel, R.M. Crooks, Langmuir 26 (2010) 1137–1146.
[16] S.U. Son, Y. Jang, J. Park, H.B. Na, H.M. Park, H.J. Yun, J. Lee, T. Hyeon, J. Am. Chem. Soc. 126 (2004) 5026–5027.
[17] S.K. Ghosh, M. Mandal, S. Kundu, S. Nath, T. Pal, Appl. Catal. A: Gen. 268 (2004) 61–66.
[18] Z.D. Pozun, S.E. Rodenbusch, E. Keller, K. Tran, W. Tang, K.J. Stevenson, G. Henkelman, J. Phys. Chem. C 117 (2013) 7598–7604.
[19] A.Y. Waddad, S. Abbad, F. Yu, W.L.L. Munyendo, J. Wang, H. Lv, J. Zhou, Int. J. Pharma. 456 (2013) 446–458.
[20] S. Rothbart, E. Ember, R. van Eldik, Dalton Trans. 39 (2010) 3264–3272.
[21] F. Polzer, S. Wunder, Y. Lu, M. Ballauff, J. Catal. 289 (2012) 80–87.
[22] M.P. Colombini, A. Andreotti, C. Baraldi, I. Degano, J.J. Łucejko, Microchem. J. 85 (2007) 174–182.
[23] A. Osman, D. Makris, Int. Food Res. J. 18 (2011).
[24] A. Masek, E. Chrzescijanska, M. Zaborski, Food Chem. 148 (2014) 18–23.
[25] S. Wunder, M. Ballauff, K. Rademann, Humboldt Universität zu Berlin, M athematisch-Naturwissenschaftliche Fakultät I, Berlin, (2012).
[26] Y.-M. Chung, H.-K. Rhee, J. Colloid Interface Sci. 271 (2004) 131–135.
[27] R. Ricciardi, J. Huskens, M. Holtkamp, U. Karst, W. Verboom, ChemCatChem 7 (2015) 877.
[28] S. Wunder, F. Polzer, Y. Lu, Y. Mei, M. Ballauff, J. Phys. Chem. C 114 (2010) 8814–8820.
[29] K. Esumi, R. Isono, T. Yoshimura, Langmuir 20 (2003) 237–243.
[30] M. Graetzel, A.J. Frank, J. Phys. Chem. 86 (1982) 2964–2967.
[31] S.-A. Ong, E. Toorisaka, M. Hirata, T. Hano, J. Hazard. Mater. 124 (2005) 88–94.
[32] A.A. Osunlaja, S.O. Idris, J.F. Iyun, Appl. Sci. Res. 4 (2012) 772–780.
[33] Q. Wang, S. Tian, P. Ning, Ind. Eng. Chem. Res. 53 (2014) 643–649.
[34] N.C. Antonels, R. Meijboom, Langmuir 29 (2013) 13433–13442.
[35] M. Nemanashi, R. Meijboom, Langmuir 31 (2015) 9041–9053.
[36] D.G. Kinniburgh, Environ. Sci. Technol. 20 (1986) 895–904.
[37] R.W. Scott, O.M. Wilson, S.-K. Oh, E.A. Kenik, R.M. Crooks, J. Am. Chem. Soc. 126 (2004) 15583–15591.
[38] Y.G. Kim, S.K. Oh, R.M. Crooks, Chem. Mater. 16 (2004) 167–172.
[39] D.V. Leff, P.C. Ohara, J.R. Heath, W.M. Gelbart, J. Phys. Chem. 99 (1995) 7036–7041.
[40] L. Chen, X. Li, J. Zhang, J. Fang, Y. Huang, P. Wang, J. Ma, Environ. Sci. Tech. 49 (2015) 10373–10379.
[41] K. Vijayaraghavan, T.V.N. Padmesh, K. Palanivelu, M. Velan, J. Hazard. Mater. B 133 (2006) 304–308.
[42] A.B. Pérez-Marín, V.M. Zapata, J.F. Ortuño, M. Aguilar, J. Sáez, M. Lloréns, J. Hazard. Mater. 139 (2007) 122–131.
[43] K. An, G.A. Somorjai, ChemCatChem 4 (2012) 1512–1524.
[44] S. Kundu, K. Wang, H. Liang, J. Phys. Chem. C 113 (2009) 5157–5163.
[45] S. Carregal-Romero, J. Pérez-Juste, P. Hervés, L.M. Liz-Marzán, P. Mulvaney, Langmuir 26 (2010) 1271–1277.
[46] A.M. Ali, E.A.C. Emanuelsson, D.A. Patterson, Appl. Catal. B: Environ. 97 (2010) 168–181.
[47] M. Petrowsky, R. Frech, J. Phys. Chem. B 113 (2009) 5996–6000.
[48] H. Eyring, Chem. Rev. 17 (1935) 65–77.